

---

# IDF++: Analyzing and Improving Integer Discrete Flows for Lossless Compression

---

Rianne van den Berg Alexey A. Gritsenko\* Mostafa Dehghani  
Casper Kaae Sønderby Tim Salimans  
{riannevdberg,agritsenko,dehghani,casperkaae,salimans}@google.com  
Google Research

## Abstract

In this paper we analyse and improve integer discrete flows for lossless compression. Integer discrete flows are a recently proposed class of models that learn invertible transformations for integer-valued random variables. Due to its discrete nature, they can be combined in a straightforward manner with entropy coding schemes for lossless compression without the need for bits-back coding. We discuss the potential difference in flexibility between invertible flows for discrete random variables and flows for continuous random variables and show that (integer) discrete flows are more flexible than previously claimed. We furthermore investigate the influence of quantization operators on optimization and gradient bias in integer discrete flows. Finally, we introduce modifications to the architecture to improve the performance of this model class for lossless compression.

## 1 Introduction

According to Shannon’s source coding theorem [43] optimal lossless compression of a data source is achieved when the expected code length is equal to the entropy of the data distribution. Density estimation algorithms that minimize the cross entropy between a data distribution and a model distribution can be interpreted as lossless compression algorithms, because the cross-entropy upper bounds the data entropy. Thus, if a density estimator matches the data distribution well, it can in principle be combined with entropy coding algorithms for lossless source compression.

Deep density estimators are particularly suitable to capture the probability distribution of high-dimensional data. Examples include autoregressive neural networks [36, 42], variational auto-encoders [26, 41, 45, 31] and normalizing flows [47, 46, 10, 41, 11, 37, 27, 21, 15, 14, 20, 17], with the latter two enjoying faster decoding times.

Variational auto-encoders can be combined with bits-back coding [16] to enable lossless compression. Even though bits-back coding requires auxiliary bits for encoding/decoding every datapoint, this cost can be reduced by encoding several datapoints, making bits-back coding algorithms suitable for compressing sequences of datapoints. Normalizing flows are sequences of invertible functions that can transform correlated random variables with multi-modal distributions to independent random variables with a simple uni-modal distribution. Most normalizing flow models are designed for real-valued continuous data, which prevents an efficient connection with entropy coders for lossless compression [19], since entropy coders require discretized data. However, normalizing flows for real-valued data were recently connected to bits-back coding by Ho et al. [18], opening up the possibility for efficient dataset compression with high compression rates. Orthogonal to this, Tran et al. [52] and Hooeboom et al. [19] introduced normalizing flows for discrete random variables.

---

\*Work completed as a Google AI Resident

Hoogeboom et al. [19] demonstrated that integer discrete flows can be connected in a straightforward manner to entropy coders without the need for bits-back coding.

In this paper we contribute to the study of normalizing flows for lossless compression as follows: i) motivated by a recent review on normalizing flows by Papamakarios et al. [38], we analyze the flexibility of normalizing flows for discrete random variables and show that they are more flexible than previously claimed; ii) we investigate the influence of quantization operators on the optimization of integer discrete flows (IDF); and iii) we introduce several architecture changes to improve the performance of this model class on lossless image compression.

## 2 Related work

**Continuous Generative Models:** Continuous generative flow-based models [8, 10, 11] are attractive due to their tractable likelihood computation. Recently these models have demonstrated promising performance in image [17, 27], audio [24] and video [29] modelling. We refer to Papamakarios et al. [38] for a recent comprehensive review of the field.

By discretizing the continuous latent vectors of such models efficient lossless compression can be achieved using bits-back coding [16]. Recent examples of such approaches are Local Bits-Back Coding with normalizing flows [18] and variational auto-encoders [26, 41] with bits-back coding such as Bits-Back with ANS [51], Bit-Swap [28] and HiLLoC [50]. These methods achieve good performance when compressing a full dataset, such as the ImageNet test set, since the auxiliary bits needed for bits-back coding can be amortized across many samples. However, encoding a single image with these methods would require more bits than the original image itself [18].

**Learned discrete lossless compression:** Producing discrete codes allows entropy coders to be directly applied to single data instances efficiently. Mentzer et al. [33] encode an image into a set of discrete multiscale latent vectors that can be stored efficiently. Fully autoregressive generative models condition unseen pixels directly on the previously observed pixel values and have achieved the best likelihood values compared to other models [36, 42]. However, decoding with these models is impractically slow since the conditional distribution for each pixel has to be decoded sequentially where each step requires a significant amount of computation. Recently, super-resolution networks were used for lossless compression [7] by storing a low resolution image in raw format and by encoding the corrections needed for lossless up-sampling to the full image resolution with a partial autoregressive model. Finally, Mentzer et al. [34] first encode an image using an efficient lossy compression algorithm and store the residual efficiently using a generative model conditioned on the lossy image encoding.

**Hand-designed Lossless Compression Codecs:** The popular PNG [6] algorithm leverages a simple autoregressive model and the DEFLATE [9] algorithm for compression. WebP [1] uses larger patches for conditional compression coupled with a custom entropy coder. In its lossless mode JPEG 2000 [39] transforms an image using wavelet transforms at multiple scales before encoding. Lastly FLIF [44] uses an adaptive entropy coder that selects the local context model using a per-image learned decision tree.

## 3 Normalizing flows

A normalizing flow consists of a sequence of invertible functions applied to a random variable  $\mathbf{x}$ :  $f^K \circ f^{K-1} \circ \dots \circ f^1(\mathbf{x})$ , yielding a sequence of random variables  $\mathbf{y}^K \leftarrow \dots \leftarrow \mathbf{y}^1 \leftarrow \mathbf{y}^0 = \mathbf{x}$ . If the probability distribution of the untransformed random variable  $\mathbf{x}$  is known, the probability distribution of the random variables  $\mathbf{y}^i$  for  $i = 1, \dots, K$  can be obtained by the change of variable formula. By parameterizing the invertible functions with invertible neural networks these models can be used to optimize the log-likelihood of  $\mathbf{y}^K$ . Flexible invertible functions can learn mappings between random variables with highly correlated dimensions and random variables with independent dimensions, as well as mappings between multi-modal distributions and uni-modal distributions.

### 3.1 Real-valued random variables

Consider a real-valued random variable  $\mathbf{x} \in \mathbb{R}^d$  with tractable distribution  $p_{\mathbf{x}}(\mathbf{x})$  from which we can sample. Let  $f : \mathbb{R}^d \mapsto \mathbb{R}^d$  be an invertible function that acts on  $\mathbf{x}$ , such that  $\mathbf{y} = f(\mathbf{x})$  is a

new random variable of the same dimensionality as  $\mathbf{x}$ :  $\mathbf{y} \in \mathbb{R}^d$ . When conditioned on  $\mathbf{x}$ ,  $\mathbf{y}$  has a conditional distribution  $p_{\mathbf{y}|\mathbf{x}}(\mathbf{y}|\mathbf{x}) = \delta(\mathbf{y} - f(\mathbf{x}))$ , where  $\delta(\cdot)$  denotes the Dirac delta function. The resulting marginal distribution of  $\mathbf{y}$  can then be obtained by marginalizing out  $\mathbf{x}$  from their joint distribution:

$$p_{\mathbf{y}}(\mathbf{y}) = \int p_{\mathbf{y}|\mathbf{x}}(\mathbf{y}|\mathbf{x})p_{\mathbf{x}}(\mathbf{x}) d\mathbf{x} = \int \delta(\mathbf{y} - f(\mathbf{x}))p_{\mathbf{x}}(\mathbf{x}) d\mathbf{x} = p_{\mathbf{x}}(f^{-1}(\mathbf{y})) \left| \det \frac{\partial \mathbf{y}}{\partial \mathbf{x}} \right|^{-1}. \quad (1)$$

The determinant of the Jacobian matrix arises due to the application of the change of variables when integrating  $\mathbf{x}$  out, and ensures that the distribution  $p_{\mathbf{y}}(\mathbf{y})$  is normalized. Repeated application of Eq. (1) then yields a simple equation for the log-probability of  $\mathbf{y}^K$ :

$$\ln p_{\mathbf{y}^K}(\mathbf{y}^K) = \ln p_{\mathbf{x}}(\mathbf{x}) - \sum_{k=1}^K \ln \left| \det \frac{\partial \mathbf{y}^k}{\partial \mathbf{y}^{k-1}} \right| \quad (2)$$

Normalizing flows for which the Jacobian determinant equals  $\pm 1$  are also referred to as volume-preserving normalizing flows. When modeling discrete data with continuous flow models, dequantization noise must be added to the input data to ensure that a lower bound to the discrete log-likelihood is optimized [53, 48, 17].

### 3.2 Discrete random variables

Next, consider  $\mathbf{x}$  to be a discrete random variable with domain  $\mathcal{X}$ , and the invertible function  $f: \mathcal{X} \mapsto \mathcal{X}$ . In general  $f$  can be a mapping between two different domains, but for our discussions it will be sufficient to consider a single domain. It is worth noting that  $\mathcal{X}$  does not need to be restricted to a set with a finite number of elements. The resulting discrete random variable  $\mathbf{y} = f(\mathbf{x})$  then has a conditional distribution represented by a Kronecker delta function:  $p_{\mathbf{y}|\mathbf{x}}(\mathbf{y}|\mathbf{x}) = \delta_{\mathbf{y}, f(\mathbf{x})}$ , with  $\delta_{i,j} = 1$  if  $i = j$  and 0 for all other cases. The marginal probability mass of  $\mathbf{y}$  then yields

$$p_{\mathbf{y}}(\mathbf{y}) = \sum_{\mathbf{x} \in \mathcal{X}} \delta_{\mathbf{y}, f(\mathbf{x})} p_{\mathbf{x}}(\mathbf{x}) = p_{\mathbf{x}}(f^{-1}(\mathbf{y})). \quad (3)$$

Note the absence of a volume correction in the form of a Jacobian determinant owing to the fact that probability mass functions only have support on a discrete set of points.

As pointed out by Papamakarios et al. [38], invertible normalizing flows for discrete random variables can only permute probability masses in the probability tensor that represents the probability distribution of the random variable. This is due to their discrete nature and a consequence of the absence of a Jacobian determinant in the change of variables formula of Eq. (3). In other words, if we have an invertible function  $f: \mathcal{X} \mapsto \mathcal{X}$ , then there is always exactly one  $\mathbf{y}$ , such that  $\mathbf{y} = f(\mathbf{x})$  and  $p_{\mathbf{x}}(\mathbf{x}) = p_{\mathbf{y}}(\mathbf{y})$ . On the contrary, non-volume preserving normalizing flows for real-valued random variables can increase or decrease the density through the Jacobian determinant in the change of variables formula in Eq. (1).

Recently, Tran et al. [52] and Hoogetboom et al. [19] have both considered normalizing flows for discrete random variables. In integer discrete flows (IDF) by Hoogetboom et al. [19] the random variables are assumed to be integers, i.e.  $\mathcal{X} = \mathbb{Z}^d$ . Utilizing the fact that integers form a group under addition, the main building block of IDF is an additive bijector in the form of a bipartite coupling layer [11]:

$$\begin{bmatrix} \mathbf{y}_a \\ \mathbf{y}_b \end{bmatrix} = \begin{bmatrix} \mathbf{x}_a \\ \mathbf{x}_b + \lfloor \mathbf{t}_{\theta}(\mathbf{x}_a) \rfloor \end{bmatrix}. \quad (4)$$

Here  $\mathbf{y}_a \in \mathbb{Z}^m$ ,  $\mathbf{y}_b \in \mathbb{Z}^n$  are obtained by splitting  $\mathbf{y} \in \mathbb{Z}^d$  into two pieces such that  $m + n = d$ , and similarly for  $\mathbf{x}_a$  and  $\mathbf{x}_b$ . As with all affine coupling layers, the inverse is simple: given  $\mathbf{y}_a$  and  $\mathbf{y}_b$ ,  $\mathbf{x}_a$  is trivially obtained as  $\mathbf{x}_a = \mathbf{y}_a$  and  $\mathbf{x}_b = \mathbf{y}_b - \lfloor \mathbf{t}_{\theta}(\mathbf{y}_a) \rfloor$ . The pre-quantized translation  $\mathbf{t}_{\theta}(\cdot)$  is represented by the output of a neural network with learnable parameters  $\theta$ . In order to ensure that the additive transformation maps integers to integers, the elements of  $\mathbf{t}_{\theta}(\mathbf{x}_a)$  are rounded to their nearest integer values with the rounding operator  $\lfloor \cdot \rfloor$ . By treating integers as a subset of real-valued numbers, and with the help of a gradient estimator, the translation network parameters  $\theta$  can be optimized with gradient-based optimizers. Hoogetboom et al. [19] use a straight-through estimator [5]: the rounding

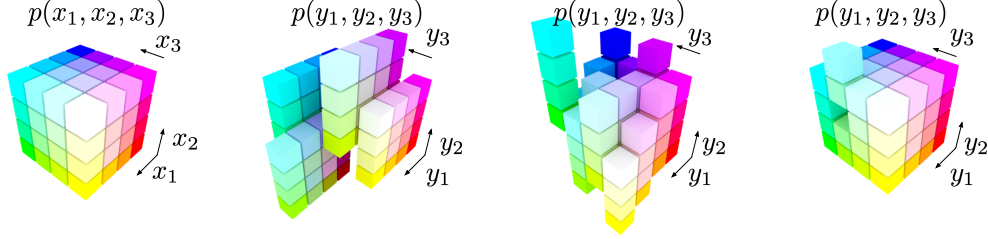


Figure 1: Left: 3D probability distribution tensor, only nonzero values are indicated with colored cubes, all empty space is assumed to be filled with zero-valued cubes. Middle left: an example of an additive transformation conditioned on  $x_3$ :  $y_1 = x_1 + \lfloor t_1(x_3) \rfloor$ ,  $y_2 = x_2 + \lfloor t_2(x_3) \rfloor$ ,  $y_3 = x_3$ . Middle right: an example of an additive transformation conditioned on  $x_1$  and  $x_3$ :  $y_1 = x_1$ ,  $y_2 = x_2 + \lfloor t_2(x_1, x_3) \rfloor$ ,  $y_3 = x_3$ . Right: a distribution tensor that a single additive transformation of the form of Eq. (4) cannot generate from the cube on the left.

operator is replaced by the identity function during back propagation. This leads to biased gradient estimates for the parameters  $\theta$ , a topic that we will come back to in section 5.

Tran et al. [52] introduce flows for discrete values that are not required to be ordinal, but which do have a finite number of possible values:  $\mathbf{x} \in \mathcal{X} = \{0, 1, \dots, K - 1\}^d$ . They introduce a bijector in the form of a coupling layer with a scale and translation and a modulo operation:  $[\mathbf{y}_a, \mathbf{y}_b] = [\mathbf{x}_a, (s_\theta(\mathbf{x}_a) \circ \mathbf{x}_b + \mathbf{t}_\theta(\mathbf{x}_a)) \bmod K]$ , with  $\circ$  denoting element-wise multiplication. The elements of the scale  $s$  and translation  $t$  are assumed to take on values in  $1, 2, \dots, K - 1$  and  $0, 1, \dots, K - 1$  respectively. The above equation is only invertible when  $s$  and  $K$  are co-prime, in which case the modular multiplicative inverse  $s^{-1}$  can be obtained through the extended Euclidean algorithm. Tran et al. [52] also introduce an autoregressive version, where  $y_i = [s_i(\mathbf{y}_{<i})x_i + t(\mathbf{y}_{<i})] \bmod K$ .

In practice, each element  $x_i$ ,  $s_i$  and  $t_i$  for  $i \in \{1, \dots, d\}$  is represented as a one-hot vector. In order to apply gradient-based methods to optimize the neural network parameters  $\theta$ , another form of a straight-through estimator is used. In the forward pass, the scale and translation are obtained by taking the argmax over the outputs of a neural net:  $s_i = \text{onehot}(\text{argmax}(\sigma_i))$ , with  $\sigma_i$  the first half of the output of a neural network:  $[\sigma_i, \tau_i] = \text{nn}_\theta(\mathbf{x}_1)$ . The one-hot translation  $t_i$  is obtained similarly from  $\tau_i$ . In the backward pass the non-differential operators are replaced with  $s_i = \text{softmax}(\sigma_i/T)$ , where  $T$  denotes a temperature parameter that determines how closely the softmax operator approximates the combined effect of the one-hot and argmax operator.

In summary, the main differences between discrete flows [52] and integer discrete flows [19] are respectively: i) a finite number of classes versus a countably infinite number of classes, ii) non-ordinal classes versus ordinal classes, iii) different straight-through estimators that approximate the respective quantization operators: one-hot quantization versus rounding. The consequence of i) and its influence on the flexibility to model arbitrary probability distributions is discussed in Section 4. The influence of quantization operators on optimization for integer discrete flows will be discussed in Section 5.

## 4 Flexibility of flows for discrete random variables

As discussed by Papamakarios et al. [38], it might seem that normalizing flows for discrete random variables are not able to model complicated distributions due to their restriction of only being able to permute the probabilities of the probability distribution tensor. This appears to be in contrast with many continuous flows that are non-volume preserving such as affine transformations [11], neural spline flows [14] and Flow++ [17]. In this section we aim to show that flows for discrete random variables are more flexible than previously claimed. We will do this by starting with an educative example as proposed by Papamakarios et al. [38].

Consider the case of a two-dimensional random variable  $\mathbf{x} = (x_1, x_2)$ , with  $x_1, x_2 \in \{0, 1\}$ , and a data-distribution given by

$$p_{\mathbf{x}}(x_1, x_2) : \begin{array}{c|cc} & x_1 \backslash x_2 & 0 & 1 \\ \hline 0 & (0.1 & 0.3) \\ 1 & (0.2 & 0.4) \end{array} . \quad (5)$$

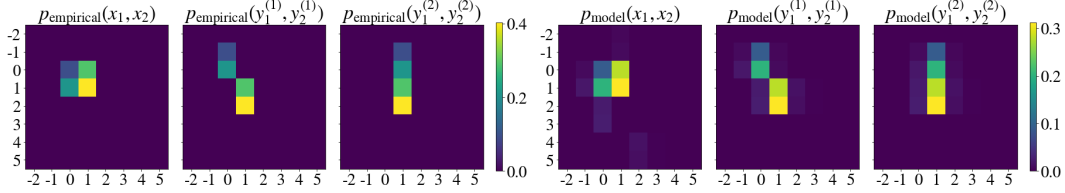


Figure 2: Visualization of an IDF that has learned the probability distribution of the toy example in Eq. (5). Left: empirical densities of the data, the data transformed by one additive bijector, and the data transformed by two additive bijectors. Right: similar to the left plot, but with data sampled from the model.

In order to map this probability distribution to an independent base distribution, the corresponding probability matrix must be of rank one. In other words, given a sequence of functions  $f^k : \mathcal{X} \mapsto \mathcal{X}$  with  $\mathcal{X} = \{0, 1\}^2$ , the probability distribution of the random variable  $\mathbf{y} = \mathbf{y}^K = f^K \circ f^{K-1} \circ \dots \circ f^1(\mathbf{x})$  should be represented by a matrix with linearly independent columns or rows, such that this matrix can be factorized into an outer product of two vectors that represent the independent base distributions for  $y_1$  and  $y_2$ . As per our discussion in Section 3, discrete flows can only permute probability mass tensors, so the matrix corresponding to  $p_{\mathbf{y}}(y_1, y_2)$  must be a permutation of the matrix in Eq. (5). Since there is no permutation of the elements in Eq. (5) that results in a rank one matrix, Papamakarios et al. [38] conclude that this is an illustrative example of a data distribution that discrete normalizing flows cannot model.

However, one of the key assumptions is that  $f^k : \mathcal{X} \mapsto \mathcal{X}$  with  $\mathcal{X} = \{0, 1\}^2$ . This example *can* in fact be solved by a normalizing flow for discrete random variables by extending  $\mathcal{X}$  to a larger number of classes. More concretely, let us extend the domain to  $\mathcal{X} = \{0, 1, 2, 3\}^2$ . The probability distribution matrix of  $\mathbf{x}$  is shown below, together with a permutation of rank 1.

$$p_{\mathbf{x}}(x_1, x_2) : \begin{pmatrix} 0.1 & 0.3 & 0 & 0 \\ 0.2 & 0.4 & 0 & 0 \\ 0 & 0 & 0 & 0 \\ 0 & 0 & 0 & 0 \end{pmatrix} \rightarrow p_{\mathbf{y}}(y_1, y_2) : \begin{pmatrix} 0.1 & 0 & 0 & 0 \\ 0.2 & 0 & 0 & 0 \\ 0.3 & 0 & 0 & 0 \\ 0.4 & 0 & 0 & 0 \end{pmatrix} = \begin{pmatrix} 0.1 \\ 0.2 \\ 0.3 \\ 0.4 \end{pmatrix} \otimes \begin{pmatrix} 1 \\ 0 \\ 0 \\ 0 \end{pmatrix}. \quad (6)$$

This example illustrates that the number of classes that are considered valid for the discrete random variables plays a crucial role in the flexibility of discrete flows. Here, we claim that this holds more generally:

**Lemma 1** *Consider any distribution over a discrete random variable of dimension  $d$  with an arbitrary dependency structure and a finite number of classes  $K$ . Bijective discrete normalizing flows can map this distribution to a base distribution which is factorized across all dimensions if the flow model takes into account a sufficiently large number of classes.*

*Furthermore, if the flow model has access to arbitrarily flexible one-dimensional learnable discrete distributions, the discrete flow model can model any such distribution.*

The “proof” is similar to the illustration in Eq. (6). Given enough classes, a factorized base distribution is obtained by “flattening” the hypercube that contains all nonzero entries in the data distribution tensor into one dimension. This is one way in which a discrete flow can factorize any distribution. However, as pointed out by Papamakarios et al. [38], a uniform base distribution will always be mapped into a uniform data distribution. Therefore, discrete flows require one-dimensional learnable distributions that are arbitrarily flexible in order to be able to model all data distributions.

Circling back to the practical implementations of flows for discrete random variables, we note that given a finite number of classes present in the data, integer discrete flows always have access to a sufficient number of classes to be able to “flatten” the data distribution due to the countably infinite number of classes in  $\mathcal{X} = \mathbb{Z}^d$ . The correct representation of the probability matrix in Eq. (5) for IDF would thus be an extension of this matrix by patching it with an infinite number of columns and rows filled with zeros.

Discrete flows as introduced by Tran et al. [52] are designed for a finite number of classes in  $\mathcal{X}$ . Although not implemented in the original work, this model class can in principle also be extended to include more classes than present in the data. In practice the number of classes will be constrained by

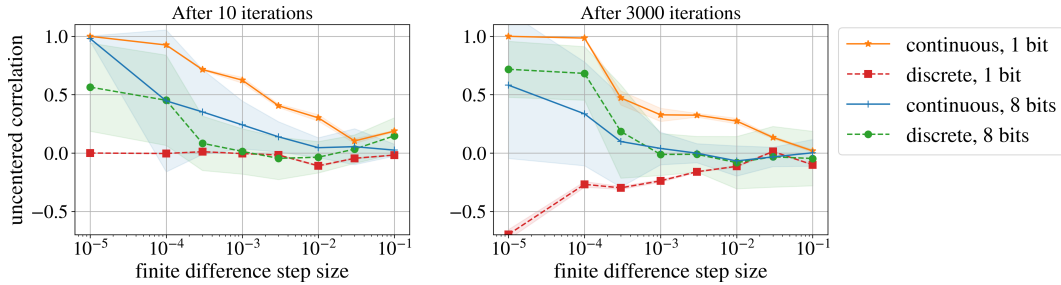


Figure 3: Agreement between approximate gradient and finite difference gradient at model initialization (left), and after 3000 training iterations (right). The curves were obtained by averaging over 10 batches. The variance for the models on 8-bit toy example is higher due to the larger number of different datapoints that exist for this dataset, leading to more variance in the data batches.

memory consumption and the quality of the gradient estimator that depends on the number of classes. As also mentioned by Tran et al. [52], previous work on Gumbel-softmax distributions indicate that the gradient approximation works well when the number of classes is lower than 200 [32, 23].

Finally, the question remains if a sequence of additive bijectors of the form of Eq. (4) can model the permutation corresponding to the flattening operator. We argue that it can by showing a visualization of the type of operations that a single additive bijector can and cannot perform on a three-dimensional probability tensor in Figure 1. Flattening any two dimensions into a single dimension will require two additive operations of the form of Eq. (4). In Figure 2 we show the probability distribution and the sequence of random variables that a trained IDF produced in order to create a factorizable distribution of the toy example in Eq. (5). As is common for toy examples studied with normalizing flows, the result is sensitive to initialization and in this case even more so due to the coarse-grained quantization that is required for the 1-bit input data.

## 5 Optimization with quantization

Hoogeboom et al. [19] argued that the performance of IDF depends on a trade-off between complexity and gradient bias introduced by the straight-through estimator. We use an extension of the toy example of Section 4 to investigate the effect of gradient bias as well as the effect of quantization on the loss landscape and optimization.

### 5.1 Gradient bias

We numerically study the significance of gradient bias on the two-dimensional example problem introduced in Section 4, solvable by a model with 3.4K parameters. We study the search directions using finite differences to approximate the gradient vector  $\mathbf{g}^{\text{fd}}$  as

$$\mathbf{g}_i^{\text{fd}} = \frac{L(\theta_i + \epsilon, \boldsymbol{\theta}_{/i}) - L(\theta_i - \epsilon, \boldsymbol{\theta}_{/i})}{2\epsilon}, \quad (7)$$

where  $L$  is our loss function averaged over a single batch of data. For additive continuous flow models (without the rounding operator and without a quantized base distribution),  $\mathbf{g}^{\text{fd}}$  will approach the true loss gradient  $\nabla_{\theta} L$  as  $\epsilon \rightarrow 0$ . For discrete models,  $\mathbf{g}^{\text{fd}}$  can be thought of as a linear approximation of the loss landscape in a trust-region of radius  $\epsilon$  around the current parameter vector  $\boldsymbol{\theta}$ . This is similar to how the straight-through gradient  $\mathbf{g}^{\text{st}}$  is used for local (trust-region) optimization when training larger flow models.

We compare continuous flow models that are trained using  $\nabla_{\theta} L$  with discrete flow models that are trained using the straight-through gradient estimator  $\mathbf{g}^{\text{st}}$ . We estimate the agreement of the gradients with the finite difference approximation  $\mathbf{g}^{\text{fd}}$  for varying trust-region size  $\epsilon$  at various stages of training and for varying bit-depth of the input data. For details on the 8-bit extension of the toy example, see Appendix A. We compute the agreement between the linear approximations using the cosine similarity  $\mathbf{g} \cdot \mathbf{g}^{\text{fd}} / \|\mathbf{g}\|_2 \|\mathbf{g}^{\text{fd}}\|_2$ , which can be interpreted as the uncentered correlation between the elements of  $\mathbf{g}$  and  $\mathbf{g}^{\text{fd}}$ . As long as the agreement between the gradient approximations is consistently positive, performing gradient descent with  $\mathbf{g}$  is expected to reduce the loss according to the trust-region approximation based on  $\mathbf{g}^{\text{fd}}$ . If the agreement is zero, or even negative, gradient descent with  $\mathbf{g}$

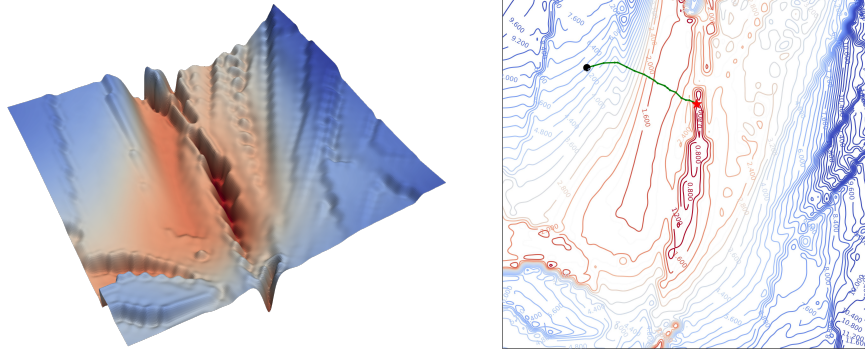


Figure 4: Visualization of the trajectory of the optimizer on the loss surface [30] for the discrete model on the 1-bit toy example.

is not expected to improve the training loss. The agreements are estimated over multiple batches. As the base distribution parameters are not affected by the gradient bias we only consider the gradients for the parameters of the bijectors.

Figure 3 shows the agreement between the finite-difference gradient and the straight-through gradient of the discrete model and the agreement with the real gradient for the continuous model, at initialization and after 3000 training iterations. We find that the discrete model for 1-bit data has the lowest correlations among all models, with the difference between the discrete and continuous model being largest after training for 3000 iterations. However, for 8-bit data the continuous and discrete models have comparable cosine similarity scores. We conclude that although gradient bias can be a problem, it is less present at higher bit-depths such as 8-bit quantized data (e.g. RGB images).

## 5.2 Loss landscape and optimizer trajectory

Navigating through a loss landscape that is affected by quantization operators can be challenging due to discontinuities. To illustrate this effect, we visualize the loss landscape and the optimization path for a successful run of the discrete model for the 1-bit toy example. We use the method proposed by Li et al. [30], where for given model parameters  $\theta^*$ , we choose two direction vectors  $\theta_1$  and  $\theta_2$  and plot the value of  $f(\alpha, \beta) = \mathcal{L}(\theta^* + \alpha\theta_1 + \beta\theta_2)$ . To choose the direction vectors, we use model parameters at different stages of training. Let  $\theta_i^*$  be model parameters after iteration  $i$ . Given the set of parameters for  $n$  iterations, we apply PCA to the matrix  $M = [\theta_0^* - \theta_n^*, \dots, \theta_{n-1}^* - \theta_n^*]$  and select the two most explanatory directions as  $\theta_1$  and  $\theta_2$ . The results for the 1-bit toy example are shown in Fig. 4 for the discrete flow model. Figure 6 in Appendix A shows similar plots for the continuous case, demonstrating a much smoother loss landscape. Fig. 4 suggests that models with unlucky initializations can easily end up in a local minima from which it is hard to escape due to sharp cliffs in the loss landscape. Figures 7 and 8 in Appendix A show a significantly less pronounced difference between the loss landscape of the continuous and discrete model for the 8-bit toy example.

## 6 Improving Integer Discrete Flows for Lossless Compression

In this section we introduce changes to the architecture of IDF that improve its performance on lossless compression. We briefly summarize the IDF architecture, for more detailed information see Appendix B. Similar to other generative flow models [11, 27], the architecture of IDF contains  $L$  levels. Each level  $l$  consists of a space-to-depth transformation followed by a sequence of  $K$  alternating channel permutations and additive coupling layers. For  $l < L$ , the output random variable of level  $l$  is split into two pieces, and only one part is further transformed by the next level:  $[z^{(l)}, \mathbf{y}^{(l)}] = f^{(l,K)} \circ \dots \circ f^{(l,1)}(\mathbf{y}^{(l-1)})$ , with  $\mathbf{y}^{(0)} = \mathbf{x}$ . Here,  $\mathbf{z} = [z^{(1)}, \dots, z^{(L)}]$  denotes the latent representation of  $\mathbf{x}$ . The distribution of  $\mathbf{z}$  for 3 levels is then factorized as  $p(\mathbf{z}) = p(z^{(1)}, z^{(2)}, z^{(3)}) = p(z^{(3)})p(z^{(2)}|\mathbf{y}^{(2)})p(z^{(1)}|\mathbf{y}^{(1)})$ , which is equivalent to  $p(z^{(3)})p(z^{(2)}|z^{(3)})p(z^{(1)}|z^{(2)}, z^{(3)})$ . The conditional distributions are modeled as discretized logistic distributions and the unconditional  $p(z^{(3)})$  is modeled with a mixture of discretized logistics with 5 components. Both the conditioning networks and the pre-quantized translations  $t_\theta$  in Eq. (4) are modeled with DenseNets [22].

Table 1: Compression results in bits per dimension (bpd) for IDF++, hand-designed codecs and other deep density estimators based on normalizing flows, super resolution and variational auto-encoders. Where available, the theoretically achievable bpd is indicated in parenthesis. Results with a \* are taken from Townsend et al. [50], and those with † are taken from Hooeboom et al. [19]. All other results are from the original papers.

Compression models	CIFAR-10	IMAGENET 32	IMAGENET 64
PNG (Boutell and Lane [6])	5.87*	6.39*	5.71*
JPEG-2000 (Rabbani [39])	5.20†	6.48†	5.10†
FLIF (Sneyers and Wuille [44])	4.19*	4.52*	4.19*
BIT-SWAP (Kingma et al. [28])	3.82 (3.78)	4.50 (4.48)	-
HiLLOc (Townsend et al. [50])	3.56 (3.55)	4.20 (4.18)	3.90 (3.89)
LBB (Ho et al. [18])	3.12 (3.12)	3.88 (3.87)	3.70 (3.70)
SREC (Cao et al. [7])	-	-	4.29
IDF (Hooeboom et al. [19])	3.34 (3.32)	4.18 (4.15)	3.90 (3.90)
IDF++	3.26 (3.24)	4.12 (4.10)	3.81 (3.81)

The first modification is to invert the channel permutations after every additive coupling layer. Although inverting the permutation after each translation does not make that part of the network more flexible, it can affect the modeling of the conditional distributions  $p(\mathbf{z}^{(l)}|\mathbf{y}^{(l)})$ . By inverting the permutations one ensures that  $\mathbf{y}^{(l)}$  and  $\mathbf{z}^{(l)}$  are the first and second half of the space-to-depth transformed version of  $\mathbf{y}^{(l-1)}$ . The second change is an adaptation of the rezero trick by Bachlechner et al. [3]. The additive bijectors of Eq. (4) are replaced by  $[\mathbf{y}_a, \mathbf{y}_b] = [\mathbf{x}_a, \mathbf{x}_b + \lfloor \alpha t_\theta(\mathbf{x}_a) \rfloor]$ , where  $\alpha$  is a learnable scalar parameter initialized to zero, such that the bijectors are initialized to the identity function. The mean and log-scale of the conditional discretized logistic distributions are parameterized as  $\boldsymbol{\mu} = \gamma \boldsymbol{\nu}$ ,  $\log s = \delta \log \boldsymbol{\sigma}$  with  $[\boldsymbol{\nu}, \log \boldsymbol{\sigma}] = \text{DenseNet}_\phi(\mathbf{y})$  and  $\gamma$  and  $\delta$  learnable scalar parameters initialized to zero. Finally, we alter the dense blocks that make up the translation and logistic conditioning DenseNets by introducing group normalization [54] layers and switching from ReLU activations [35] to Swish activations [40]:

IDF: Conv1x1  $\rightarrow$  ReLU  $\rightarrow$  Conv3x3  $\rightarrow$  ReLU

IDF++: Conv1x1  $\rightarrow$  GroupNorm  $\rightarrow$  Swish  $\rightarrow$  Conv3x3  $\rightarrow$  GroupNorm  $\rightarrow$  Swish

The combination of the rezero trick and the group normalization layers allows for the use of a higher base learning rate. We furthermore use an exponential moving average for evaluation.

To make a fair comparison against other methods like local bits-back coding (LBB) by Ho et al. [18] we train our final models on the entire training set without holding out part of the training set as a validation set. Although there is no visible difference for the ImageNet32 and ImageNet64 datasets, more data does matter for Cifar-10: it reduces the theoretical average negative log-likelihood in units of bits per dimension (bpd) on the test set from 3.32 to 3.30 for the baseline IDF model. Table 1 displays the practically achieved bpd after compression. Results for hand-designed codecs, models with bits-back coding and models without bits-back coding are shown in separate groups. Where available, theoretically achievable bpd is indicated in brackets. The results show that the modifications proposed in IDF++ improve the performance over IDF for all datasets. For a more detailed ablation on the contributions of the proposed modifications see Appendix C.

Recent research shows that numerically inverting continuous flow models can lead to instabilities and lossy inversion [4], especially for affine flow models. This would be particularly problematic for applications such as lossless compression where it corresponds to lossy decompression. At present it is unclear to what extent this affects LBB [18]. However, IDFs are composed of additive bijectors with rounding operators that ensure integer addition, and thus we observed that numerical inversion results in exactly zero reconstruction errors, even for deep models.

## 7 Conclusion

We have analyzed the flexibility of normalizing flows for discrete random variables and investigated the effect of the rounding operator and the straight-through estimator for IDF. Furthermore, we



introduced architecture changes to improve the compression performance of IDF. An important direction for future work is to reduce the computational complexity of deep density estimators. Although hand-designed codecs such as JPEG-2000 do not compress as well on the datasets we consider, they (de)compress significantly faster and require significantly less memory while not being tuned for each dataset. More work in directions like optimizing for (de)compression speed [7] or generalizing learnable compressors to other datasets [50] is needed to make deep density estimators more practical for source compression.

## Broader Impact

Designing efficient algorithms that achieve high compression rates is relevant because of the large amount of data generated every day. While many applications allow for lossy data compression, some applications require lossless storage of data. A prominent and classic example is medical data for which lossless storage is critical. As mentioned above, an important avenue for future research is to reduce the computational demands while maintaining good compression performance. This could for instance allow for (de)compression on handheld devices such as smart phones. As generative models, normalizing flows are susceptible to harmful inductive biases and dataset biases. Among other things they can also be misused to create fake data.

## Acknowledgments and Disclosure of Funding

We would like to thank Nal Kalchbrenner and Patrick Forré for useful discussions during the project and Lucas Theis for feedback on our manuscript.

## References

- [1] WebP Image format. URL <https://developers.google.com/speed/webp/>.
- [2] Martín Abadi, Ashish Agarwal, Paul Barham, Eugene Brevdo, Zhifeng Chen, Craig Citro, Greg S. Corrado, Andy Davis, Jeffrey Dean, Matthieu Devin, Sanjay Ghemawat, Ian Goodfellow, Andrew Harp, Geoffrey Irving, Michael Isard, Yangqing Jia, Rafal Jozefowicz, Lukasz Kaiser, Manjunath Kudlur, Josh Levenberg, Dandelion Mané, Rajat Monga, Sherry Moore, Derek Murray, Chris Olah, Mike Schuster, Jonathon Shlens, Benoit Steiner, Ilya Sutskever, Kunal Talwar, Paul Tucker, Vincent Vanhoucke, Vijay Vasudevan, Fernanda Viégas, Oriol Vinyals, Pete Warden, Martin Wattenberg, Martin Wicke, Yuan Yu, and Xiaoqiang Zheng. TensorFlow: Large-scale machine learning on heterogeneous systems, 2015. URL <https://www.tensorflow.org/>. Software available from [tensorflow.org](https://www.tensorflow.org/).
- [3] Thomas Bachlechner, Bodhisattwa Prasad Majumder, Huanru Henry Mao, Garrison W. Cottrell, and Julian McAuley. ReZero is All You Need: Fast Convergence at Large Depth, 2020.
- [4] Jens Behrmann, Paul Vicol, Kuan-Chieh Wang, Roger Grosse, and Jörn-Henrik Jacobsen. Understanding and mitigating exploding inverses in invertible neural networks, 2020.
- [5] Yoshua Bengio, Nicholas Léonard, and Aaron Courville. Estimating or propagating gradients through stochastic neurons for conditional computation. *arXiv preprint arXiv:1308.3432*, 2013.
- [6] Thomas Boutell and T Lane. PNG (portable network graphics) specification version 1.0. *Network Working Group*, pages 1–102, 1997.
- [7] Sheng Cao, Chao-Yuan Wu, and Philipp Krähenbühl. Lossless Image Compression through Super-Resolution. *arXiv preprint arXiv:2004.02872*, 2020.
- [8] Scott Saobing Chen and Ramesh A. Gopinath. Gaussianization. In T. K. Leen, T. G. Dietterich, and V. Tresp, editors, *Advances in Neural Information Processing Systems 13*, pages 423–429. MIT Press, 2001. URL <http://papers.nips.cc/paper/1856-gaussianization.pdf>.
- [9] Peter Deutsch. DEFLATE compressed data format specification version 1.3, 1996.
- [10] Laurent Dinh, David Krueger, and Yoshua Bengio. NICE: Non-linear independent components estimation. *arXiv preprint arXiv:1410.8516*, 2014.

- [11] Laurent Dinh, Jascha Sohl-Dickstein, and Samy Bengio. Density estimation using real NVP. *arXiv preprint arXiv:1605.08803*, 2016.
- [12] Jarek Duda. Asymmetric numeral systems, 2009.
- [13] Jarek Duda. Asymmetric numeral systems: entropy coding combining speed of huffman coding with compression rate of arithmetic coding, 2013.
- [14] Conor Durkan, Artur Bekasov, Iain Murray, and George Papamakarios. Neural Spline Flows. In *Advances in Neural Information Processing Systems 32*, pages 7509–7520. Curran Associates, Inc., 2019.
- [15] Will Grathwohl, Ricky T. Q. Chen, Jesse Bettencourt, and David Duvenaud. Scalable Reversible Generative Models with Free-form Continuous Dynamics. In *International Conference on Learning Representations*, 2019.
- [16] Geoffrey E Hinton and Drew Van Camp. Keeping the neural networks simple by minimizing the description length of the weights. In *Proceedings of the sixth annual conference on Computational learning theory*, pages 5–13, 1993.
- [17] Jonathan Ho, Xi Chen, Aravind Srinivas, Yan Duan, and Pieter Abbeel. Flow++: Improving flow-based generative models with variational dequantization and architecture design. *arXiv preprint arXiv:1902.00275*, 2019.
- [18] Jonathan Ho, Evan Lohn, and Pieter Abbeel. Compression with Flows via Local Bits-Back Coding. In *Advances in Neural Information Processing Systems 32*, pages 3879–3888, 2019.
- [19] Emiel Hoogeboom, Jorn Peters, Rianne van den Berg, and Max Welling. Integer Discrete Flows and Lossless Compression. In *Advances in Neural Information Processing Systems 32*, pages 12134–12144. Curran Associates, Inc., 2019.
- [20] Emiel Hoogeboom, Rianne Van Den Berg, and Max Welling. Emerging Convolutions for Generative Normalizing Flows. In *Proceedings of the 36th International Conference on Machine Learning*, 2019.
- [21] Chin-Wei Huang, David Krueger, Alexandre Lacoste, and Aaron Courville. Neural Autoregressive Flows. In *Proceedings of the 35th International Conference on Machine Learning*, Proceedings of Machine Learning Research, 2018.
- [22] G. Huang, Z. Liu, L. Van Der Maaten, and K. Q. Weinberger. Densely Connected Convolutional Networks. In *2017 IEEE Conference on Computer Vision and Pattern Recognition (CVPR)*, pages 2261–2269, 2017.
- [23] Eric Jang, Shixiang Gu, and Ben Poole. Categorical Reparameterization with Gumbel-Softmax. In *International Conference on Learning Representations*, 2017.
- [24] Sungwon Kim, Sang-gil Lee, Jongyoon Song, Jaehyeon Kim, and Sungroh Yoon. FloWaveNet: A generative flow for raw audio. *arXiv preprint arXiv:1811.02155*, 2018.
- [25] Diederik P. Kingma and Jimmy Ba. Adam: A method for stochastic optimization, 2014.
- [26] Diederik P Kingma and Max Welling. Auto-encoding variational bayes. *arXiv preprint arXiv:1312.6114*, 2013.
- [27] Durk P Kingma and Prafulla Dhariwal. Glow: Generative flow with invertible 1x1 convolutions. In *Advances in Neural Information Processing Systems*, pages 10215–10224, 2018.
- [28] Friso H Kingma, Pieter Abbeel, and Jonathan Ho. Bit-swap: Recursive bits-back coding for lossless compression with hierarchical latent variables. *arXiv preprint arXiv:1905.06845*, 2019.
- [29] Manoj Kumar, Mohammad Babaeizadeh, Dumitru Erhan, Chelsea Finn, Sergey Levine, Laurent Dinh, and Durk Kingma. Videoflow: A flow-based generative model for video. *arXiv preprint arXiv:1903.01434*, 2019.

- [30] Hao Li, Zheng Xu, Gavin Taylor, Christoph Studer, and Tom Goldstein. Visualizing the loss landscape of neural nets. In *Advances in Neural Information Processing Systems*, pages 6389–6399, 2018.
- [31] Lars Maaløe, Marco Fraccaro, Valentin Liévin, and Ole Winther. BIVA: A Very Deep Hierarchy of Latent Variables for Generative Modeling, 2019.
- [32] Chris J. Maddison, Andriy Mnih, and Yee Whye Teh. The Concrete Distribution: A Continuous Relaxation of Discrete Random Variables. In *International Conference on Learning Representations*, 2017.
- [33] Fabian Mentzer, Eirikur Agustsson, Michael Tschannen, Radu Timofte, and Luc Van Gool. Practical full resolution learned lossless image compression. In *Proceedings of the IEEE Conference on Computer Vision and Pattern Recognition*, pages 10629–10638, 2019.
- [34] Fabian Mentzer, Luc Van Gool, and Michael Tschannen. Learning Better Lossless Compression Using Lossy Compression. *arXiv preprint arXiv:2003.10184*, 2020.
- [35] Vinod Nair and Geoffrey E. Hinton. Rectified Linear Units Improve Restricted Boltzmann Machines. In *Proceedings of the 27th International Conference on International Conference on Machine Learning*, 2010.
- [36] Aaron van den Oord, Nal Kalchbrenner, and Koray Kavukcuoglu. Pixel recurrent neural networks. *arXiv preprint arXiv:1601.06759*, 2016.
- [37] George Papamakarios, Theo Pavlakou, and Iain Murray. Masked Autoregressive Flow for Density Estimation. In *Advances in Neural Information Processing Systems 30*, 2017.
- [38] George Papamakarios, Eric Nalisnick, Danilo Jimenez Rezende, Shakir Mohamed, and Balaji Lakshminarayanan. Normalizing Flows for Probabilistic Modeling and Inference, 2019.
- [39] Majid Rabbani. JPEG2000: Image compression fundamentals, standards and practice. *Journal of Electronic Imaging*, 11(2):286, 2002.
- [40] Prajit Ramachandran, Barret Zoph, and Quoc V. Le. Searching for Activation Functions, 2017.
- [41] Danilo Rezende and Shakir Mohamed. Variational Inference with Normalizing Flows. In *Proceedings of the 32nd International Conference on Machine Learning*, 2015.
- [42] Tim Salimans, Andrej Karpathy, Xi Chen, and Diederik P Kingma. PixelCNN++: Improving the PixelCNN with discretized logistic mixture likelihood and other modifications. *arXiv preprint arXiv:1701.05517*, 2017.
- [43] Claude E Shannon. A mathematical theory of communication. *Bell system technical journal*, 27(3):379–423, 1948.
- [44] Jon Sneyers and Pieter Wuille. FLIF: Free lossless image format based on MANIAC compression. In *2016 IEEE International Conference on Image Processing (ICIP)*, pages 66–70. IEEE, 2016.
- [45] Casper Kaae Sønderby, Tapani Raiko, Lars Maaløe, Søren Kaae Sønderby, and Ole Winther. Ladder Variational Autoencoders. In *Advances in Neural Information Processing Systems 29*, 2016.
- [46] Esteban G Tabak and Cristina V Turner. A family of nonparametric density estimation algorithms. *Communications on Pure and Applied Mathematics*, 66(2):145–164, 2013.
- [47] Esteban G Tabak, Eric Vanden-Eijnden, et al. Density estimation by dual ascent of the log-likelihood. *Communications in Mathematical Sciences*, 8(1):217–233, 2010.
- [48] Lucas Theis, Aäron van den Oord, and Matthias Bethge. A note on the evaluation of generative models, 2015.
- [49] James Townsend. A tutorial on the range variant of asymmetric numeral systems, 2020.

- [50] James Townsend, Thomas Bird, Julius Kunze, and David Barber. HiLLOc: Lossless Image Compression with Hierarchical Latent Variable Models. *arXiv preprint arXiv:1912.09953*, 2019.
- [51] James Townsend, Tom Bird, and David Barber. Practical lossless compression with latent variables using bits back coding. *arXiv preprint arXiv:1901.04866*, 2019.
- [52] Dustin Tran, Keyon Vafa, Kumar Agrawal, Laurent Dinh, and Ben Poole. Discrete Flows: Invertible Generative Models of Discrete Data. In *Advances in Neural Information Processing Systems 32*, pages 14692–14701, 2019.
- [53] Benigno Uria, Iain Murray, and Hugo Larochelle. RNADE: The real-valued neural autoregressive density-estimator. In C. J. C. Burges, L. Bottou, M. Welling, Z. Ghahramani, and K. Q. Weinberger, editors, *Advances in Neural Information Processing Systems 26*, pages 2175–2183. Curran Associates, Inc., 2013. URL <http://papers.nips.cc/paper/5060-rnade-the-real-valued-neural-autoregressive-density-estimator.pdf>.
- [54] Yuxin Wu and Kaiming He. Group Normalization. *Lecture Notes in Computer Science*, page 3–19, 2018. ISSN 1611-3349. doi: 10.1007/978-3-030-01261-8\_1. URL [http://dx.doi.org/10.1007/978-3-030-01261-8\\_1](http://dx.doi.org/10.1007/978-3-030-01261-8_1).

# Supplementary Material of “IDF++: Analyzing and Improving Integer Discrete Flows for Lossless Compression”

## Appendix A Learning toy examples

### A.1 Extension of the toy example

The toy example that is discussed in Section 4 has a probability distribution with nonzero probabilities for  $x_i \in \{0, 1\}$ . With only two values per dimension with nonzero probability, the data is effectively 1-bit quantized. In Section 5 we use an extension of this toy example for input data that is quantized to a higher bit-depth. This can be done by modeling the probability masses with log-linearly spaced logits in the interval  $(0, 1)$ . The resulting distributions for several bit-depths are shown in Fig. 5.

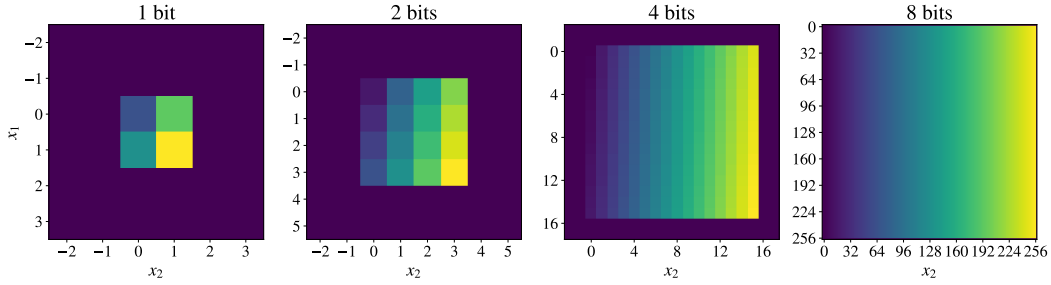


Figure 5: probability distribution of the extension of the toy example of Eq. (5) to more bits.

### A.2 Analytical solution for the toy examples

Factorizing the distribution matrix of the toy example in Eq. (5) can be done with two translations:

$$\begin{aligned}
 \text{(1)} \quad & \begin{cases} y_1^{(1)} = x_1 + t(x_2) \\ y_2^{(1)} = x_2 \end{cases} \quad \text{with} \quad t(x_2) = \begin{cases} 0, & \text{if } x_2 = 0 \\ 2, & \text{if } x_2 = 1 \end{cases} \\
 \text{(2)} \quad & \begin{cases} y_1^{(2)} = y_1^{(1)} \\ y_2^{(2)} = y_2^{(1)} + \bar{t}(y_1^{(1)}) \end{cases} \quad \text{with} \quad \bar{t}(y_1^{(1)}) = \begin{cases} 0, & \text{if } y_1^{(1)} \in \{0, 1\} \\ -1, & \text{if } y_1^{(1)} \in \{2, 3\} \end{cases} .
 \end{aligned}$$

For other values of  $x_2$  and  $y_1^{(1)}$  the values of  $t(x_2)$  and  $\bar{t}(y_1^{(1)})$  are unrestricted. For the extension of the toy example to  $n$  bits, two translations also suffice:

$$\begin{aligned}
 \text{(1)} \quad & \begin{cases} y_1^{(1)} = x_1 + t(x_2) \\ y_2^{(1)} = x_2 \end{cases} \quad \text{with} \quad t(x_2) = x_2 \times 2^n \\
 \text{(2)} \quad & \begin{cases} y_1^{(2)} = y_1^{(1)} \\ y_2^{(2)} = y_2^{(1)} + \bar{t}(y_1^{(1)}) \end{cases} \quad \text{with} \quad \bar{t}(y_1^{(1)}) = -\text{floor}(y_1^{(1)}/2^n) .
 \end{aligned}$$

Similarly, two dimensions of a  $d$ -dimensional probability tensor can be “flattened” by two translation operations.

### A.3 Visualizing the loss surface

In Section 5.2, we presented the visualization of the loss landscape and the optimization trajectory of the *discrete* model on a toy example with 1-bit data. Figure 6 presents the loss landscape and the optimization path of a *continuous* model, trained on 1-bit data. Comparing this to Figure 4, which shows the discrete model, we see that the discontinuities in the loss landscape are no longer present.

Figures 7 and 8 show the loss landscape and the optimizer path on a toy example with 8-bit data, for a discrete and a continuous model, respectively. Although the loss landscape of the discrete model is not as smooth as the continuous model, optimization seems less challenging compared to the toy

example with 1-bit data. This supports our observation in Section 5.1 that the gradient bias is less of an issue at higher bit-depths.

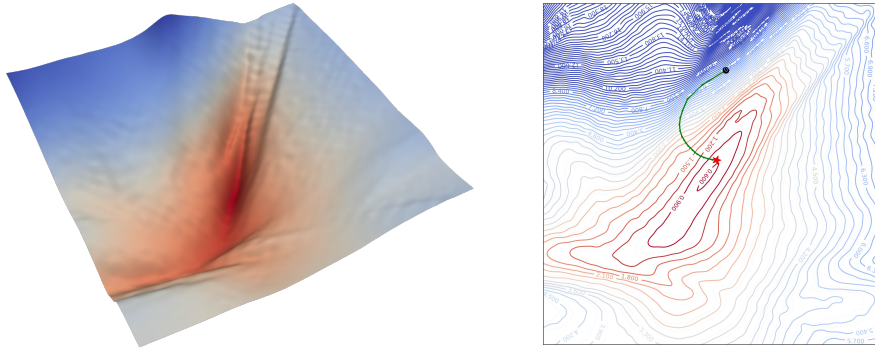


Figure 6: Visualization of the trajectory of the optimization on the loss surface [30] for the continuous model for the toy example with 1-bit data.

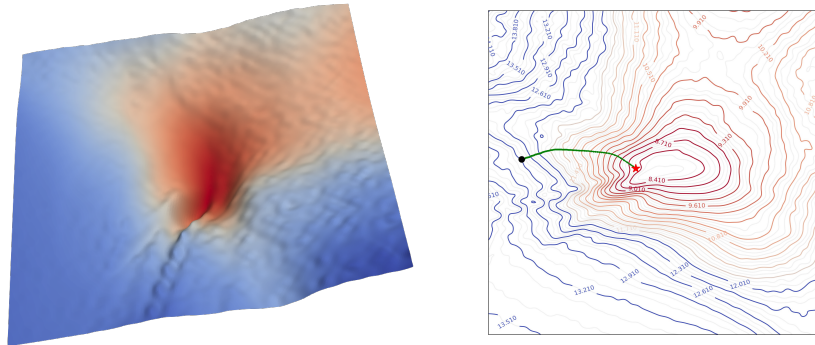


Figure 7: Visualization of the trajectory of the optimization on the loss surface [30] for the discrete model for the toy example with 8-bit data.

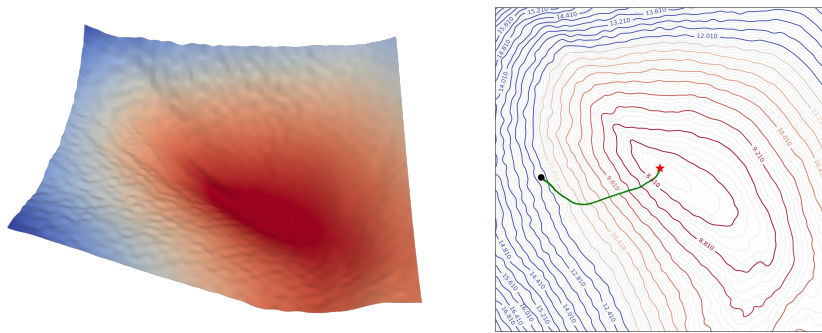


Figure 8: Visualization of the trajectory of the optimization on the loss surface [30] for the continuous model for the toy example with 8-bit data.

## Appendix B Architecture

### B.1 Architecture and training details of IDF

The architecture of IDF consists of  $L$  levels, each consisting of an alternating sequence of channel permutations and additive bijectors. More specifically, the architecture of level  $l$  of IDF is built up as

follows:

$$\mathbf{y}^{(l-1)} \rightarrow \text{space-to-depth} \rightarrow \overbrace{\{\text{Permute} \rightarrow \text{Additive transform}\}}^{\times K} \rightarrow [\mathbf{z}^{(l)}, \mathbf{y}^{(l)}].$$

Except for the last level, the output random variable is split into two equal halves  $[\mathbf{z}^{(l)}, \mathbf{y}^{(l)}]$ , where only  $\mathbf{y}^{(l)}$  is transformed by the next level. Furthermore,  $\mathbf{y}^{(0)} = \mathbf{x}$  and  $\mathbf{z} = [\mathbf{z}^{(1)}, \dots, \mathbf{z}^{(L)}]$  denotes the latent representation of  $\mathbf{x}$ . Inside the additive transformations of Eq. (4) the prequantized translations are modeled using DenseNets [22] with dense blocks of the following structure:

$$\text{Dense block: Conv1x1} \rightarrow \text{ReLU} \rightarrow \text{Conv3x3} \rightarrow \text{ReLU}.$$

All DenseNets have a depth of 12 blocks and 512 channels. The additive bijector splits the random variable into two parts along the channel dimension with splitting fractions 3/4 and 1/4 for the untransformed and transformed parts of the random variable. After translating, the resulting variables are concatenated again along the channel axis.

The distribution of  $\mathbf{z}$  for  $L$  levels is factorized as  $p(\mathbf{z}) = p(\mathbf{z}^{(L)})p(\mathbf{z}^{(L-1)}|\mathbf{y}^{(L-1)}) \dots p(\mathbf{z}^{(1)}|\mathbf{y}^{(1)})$ , which is equivalent to  $p(\mathbf{z}^{(L)})p(\mathbf{z}^{(L-1)}|\mathbf{z}^{(L)}) \dots p(\mathbf{z}^{(1)}|\mathbf{z}^{(2)}, \dots, \mathbf{z}^{(L)})$ . All conditional distributions are modeled with discretized logistic distributions. The unconditional distribution  $p(\mathbf{z}^{(L)})$  is modeled with a mixture of discretized logistics with five components. The log-scale and mean of the conditional logistic distributions are modeled as the outputs of DenseNets with the same structure as the DenseNets of the prequantized translations:  $[\nu, \log \sigma] = \text{DenseNet}_\phi(\mathbf{y})$ . Note that instead of modeling the random variables as integers ( $\mathbf{x} \in \mathbb{Z}^d$ ), they are modeled as discrete random variables on a grid with bin-width 1/256 ( $\mathbf{x} \in \mathbb{Z}^d/256$ ).

The model is trained with the Adamax optimizer [25] with an exponential learning rate schedule with base learning rate equal to  $1 \times 10^{-3}$  and a linear warmup phase of 10 epochs. See Table 2 for more details on the learning rate decay, the number of levels, the batch size and the number of epochs used for training.

Table 2: Architecture and training settings for IDF. Table adapted from Hooageboom et al. [19]. Note that we used a batch size of 128 for Cifar-10 instead of 256 as used in the original work, while still reproducing the same number as reported by Hooageboom et al. [19]. For ImageNet 32 and ImageNet 64 the batch sizes are the same as in the original work [19].

Dataset	Levels $L$	Batch size	lr decay	Epochs
Cifar-10	3	128	0.999	2000
ImageNet 32	3	256	0.99	100
ImageNet 64	4	64	0.99	10

Range-based Asymmetric Numerical Systems (rANS) [12, 13, 49] is used for lossless compression of the latent variables  $\mathbf{z} = [\mathbf{z}^{(1)}, \dots, \mathbf{z}^{(L)}]$  by using the probability distribution  $p(\mathbf{z}) = p(\mathbf{z}^{(L)})p(\mathbf{z}^{(L-1)}|\mathbf{y}^{(L-1)}) \dots p(\mathbf{z}^{(1)}|\mathbf{y}^{(1)})$  corresponding to the model’s multi-level structure.

## B.2 Architecture and training details of IDF++

In IDF++, each of the  $K$  blocks containing a permutation and additive bijector has an additional inverse channel permutation to ensure that the output random variable has the same spatial and channel ordering as the input random variable:

$$\mathbf{y}^{(l-1)} \rightarrow \text{space-to-depth} \rightarrow \overbrace{\{\text{Permute} \rightarrow \text{Additive transform} \rightarrow \text{Inverse permute}\}}^{\times K} \rightarrow [\mathbf{z}^{(l)}, \mathbf{y}^{(l)}].$$

The dense blocks of the DenseNets for the prequantized translations and the conditional discretized logistics have additional group normalization layers [54] and Swish activations [40] instead of ReLU activations [35]:

$$\text{Dense block: Conv1x1} \rightarrow \text{GroupNorm} \rightarrow \text{Swish} \rightarrow \text{Conv3x3} \rightarrow \text{GroupNorm} \rightarrow \text{Swish}.$$

The number of groups for each group normalization layer are determined as follows: if the number of channels of the group normalization layer is divisible by 3 then 3 groups are used, else if it is divisible by 2 then 2 groups are used, and finally if it is neither divisible by 3 or 2 then a single group is used.

The additive bijectors of Eq. (4) are adjusted to include a learnable scalar parameter that ensures initialization to the identity operator, similar to the rezero trick by Bachlechner et al. [3]:

$$\begin{bmatrix} \mathbf{y}_a \\ \mathbf{y}_b \end{bmatrix} = \begin{bmatrix} \mathbf{x}_a \\ \mathbf{x}_b + [\mathbf{t}_\theta(\alpha \mathbf{x}_a)] \end{bmatrix}. \quad (8)$$

Here  $\alpha$  is a learnable scalar parameter initialized to zero. The mean and log-scale of the conditional discretized logistic distributions are parameterized as  $\boldsymbol{\mu} = \gamma \boldsymbol{\nu}$ ,  $\log \mathbf{s} = \delta \log \boldsymbol{\sigma}$  with  $[\boldsymbol{\nu}, \log \boldsymbol{\sigma}] = \text{DenseNet}_\phi(\mathbf{y})$ .  $\gamma$  and  $\delta$  are learnable scalar parameters initialized to zero, such that the scale is initialized to one and the mean is initialized to zero.

The combination of the rezero trick and the group normalization layers allows us to use a larger base learning rate of  $2 \times 10^{-3}$  in the exponential decayed learning rate schedule. For Cifar-10, IDF++ was trained for 1400 epochs instead of 2000 epochs as overfitting was observed for more epochs. We evaluated all variations of IDF with an exponential moving average of the trainable parameters with a decay rate of 0.9999.

### B.3 Datasets

The training set of Cifar-10 consists of 50000 images and the test set contains 10000 images. ImageNet 32 and ImageNet 64 contain approximately 1250000 train images and 50000 test images. While we used a validation set that was held out from the respective training sets for model development, we trained our final models on the entire training set for each dataset. The effect of this is discussed in Section C. We follow Hooeboom et al. [19] and augment the Cifar-10 dataset with horizontal flipping, reflect-padding and random cropping during training. No augmentation is used for ImageNet 32 and ImageNet64.

### B.4 Hardware and software

We implemented our models in TensorFlow [2]. The majority of experiments were run with 8 NVIDIA V100 GPUs. The ImageNet64 results were produced with v3 Cloud TPUs with 8-way data parallelism.

## Appendix C Ablation study

Table 3 shows the contributions of the modifications proposed in Section 6 for IDF++. As Hooeboom et al. [19] only use 80% of the training data for Cifar-10, we also show the influence of using the entire train set for training, as opposed to keeping 20% held out as a validation set. Note that the result for the original IDF model on 80% of the training data reproduces the result of Hooeboom et al. [19]. The held out validation set for ImageNet32 and ImageNet64 was much smaller and we noticed no significant change in performance when training on the entire training set for these datasets. All models without group normalization were trained for 2000 epochs. The final IDF++ model, which includes group normalization layers, was trained for 1400 epochs to avoid overfitting.

Table 3: Ablation study of the modifications of IDF for the Cifar-10 dataset. The second column indicates the percentage of the dataset’s original train set that was used to train the model. EMA = exponential moving average. The reported numbers are theoretically achievable bits per dimension.

IDF variations	% Train data	CIFAR-10
IDF	80%	3.322
IDF	100%	3.298
IDF + EMA	100%	3.291
IDF + EMA + rezero + lr $\times$ 2	100%	3.262
IDF + EMA + rezero + lr $\times$ 2 + invert perm	100%	3.255
IDF + EMA + rezero + lr $\times$ 2 + invert perm + groupnorm ( <b>IDF++</b> )	100%	3.241